HHS Public Access

Author manuscript

Wiley Interdiscip Rev Syst Biol Med. Author manuscript; available in PMC 2020 November 01.

Published in final edited form as:

Wiley Interdiscip Rev Syst Biol Med. 2020 November ; 12(6): e1501. doi:10.1002/wsbm.1501.

Mammalian cell and tissue imaging using Raman and coherent Raman microscopy

Anthony A. Fung, **Lingyan Shi**

Department of Bioengineering, University of California San Diego, La Jolla, California

Abstract

Direct imaging of metabolism in cells or multicellular organisms is important for understanding many biological processes. Raman scattering (RS) microscopy, particularly, coherent Raman scattering (CRS) such as coherent anti-Stokes Raman scattering (CARS) and stimulated Raman scattering (SRS), has emerged as a powerful platform for cellular imaging due to its high chemical selectivity, sensitivity, and imaging speed. RS microscopy has been extensively used for the identification of subcellular structures, metabolic observation, and phenotypic characterization. Conjugating RS modalities with other techniques such as fluorescence or infrared (IR) spectroscopy, flow cytometry, and RNA-sequencing can further extend the applications of RS imaging in microbiology, system biology, neurology, tumor biology and more. Here we overview RS modalities and techniques for mammalian cell and tissue imaging, with a focus on the advances and applications of CARS and SRS microscopy, for a better understanding of the metabolism and dynamics of lipids, protein, glucose, and nucleic acids in mammalian cells and tissues.

Keywords

coherent Raman; glucose; lipid; mammalian cell; metabolism; nucleic acid; optical imaging; protein; Raman scattering; stimulated Raman

1 | INTRODUCTION

Raman scattering (RS) is the inelastic scattering of visible monochromatic light, during which a quantum of energy from a photon induces vibration in molecular bonds. Given incident light of certain wavelength, different molecular bonds within an analyte will vibrate at different frequencies, allotting each molecular bond a distinct “fingerprint,” and each molecular bond’s vibrational frequency requires specific quanta of energy from incident photons. Since the light is not absorbed by the substance, the photons are then scattered, having an energy (wavelength) different from incident photons. The change in wavelength

Correspondence: Lingyan Shi, Department of Bioengineering, University of California San Diego, La Jolla, CA 92093. lingyanshi@ucsd.edu.

AUTHOR CONTRIBUTIONS

Anthony A. Fung: Writing and editing the original manuscript. **Lingyan Shi:** Conceiving the concepts, writing and editing the original manuscript, securing funding.

CONFLICT OF INTEREST

The author has declared no conflicts of interest for this article.

between the incident and scattered light is called Raman shift. A Raman shift may be either a negative or positive shift in energy, referred to as Stokes or anti-Stokes, respectively. The Raman shift is directly related to the energy required to vibrate the molecular bonds in the analyte. Higher Raman signal intensities and peaks indicate a greater concentration of bonds with certain vibrational frequencies. The theory of RS is well documented and reviewed by Prince, Frontiera, & Potma, 2017, Jones, Hooper, Zhang, Wolverson, & Valev, 2019, and Auner et al., 2018.

At the atomic level, electrons of the analyte are placed in a short-lived virtual energy state, inducing a dipole moment as a simple consequence of electron repulsion. Since RS depends on the polarizability of a molecular bond, in contrast to how polar a bond may already be, as in the case of infrared (IR) spectroscopy, molecules with a weaker IR signal may have a stronger RS signal (Bernath, 2005). That is, substances with weak intrinsic dipole moments can be analyzed by their chemical structure. This phenomenon makes Raman spectroscopy an excellent tool for biological research, in which the non- or weakly-polar organic compounds are of interest. Additionally, photons are not emitted from the analyte when its molecules return to a lower electronic energy state, as in fluorescence-based methods. This allows for the direct tuning of incident laser light to a specific chemical structure, while avoiding the employ of large hydrophobic fluorophores that may affect the distribution and function of a conjugated analyte. Thus, Raman spectroscopy is attractive to many researchers as an imaging tool for the identification and has been widely used in life science in the past decades.

There are many variations of RS, those most often used in biology and life science include spontaneous RS, resonant RS, surface-enhanced Raman scattering (SERS), coherent anti-Stokes Raman scattering (CARS), and stimulated Raman scattering (SRS). Spontaneous Raman is the normal RS, which has been widely used to investigate complex molecular systems such as cells and tissues. However, applying spontaneous Raman for live cell/tissue imaging is challenging due to its weak intensity (the cross section is as small as ~10^{-30} cm^2) that needs a long imaging time for even tens of minutes per frame (Yue & Cheng, 2016). In SERS, the RS signal is significantly increased (10^7 times) and the detection resolution can reach single-molecule levels in simple analytes such as organic crystals (Blackie, Le Ru, & Etchegoin, 2009) and proteins (Almehmadi, Curley, Tokranova, Tenenbaum, & Lednev, 2019) in homogenous bulk or metal surfaces. The enhancement of SERS is achieved majorly due to surface plasmon resonance in a noble metal (usually silver or gold) nanostructures. CARS and SRS nonlinear optical process, achieved by using two spatially and temporally synchronized pulsed lasers, one as the pump (ω_p) beam and the other Stokes (ω_s) beam. When the frequency difference ($\omega_p - \omega_s$) between the pump beam and Stokes beam matches a molecule's vibration frequency, four processes occur: coherent RS, coherent anti-Stokes at ($2\omega_p - \omega_s$), stimulated Raman gain (SRG) at the Stokes beam, and stimulated Raman loss (SRL) at the pump beam. Although a species of interest has its own unique Raman spectrum, only certain areas along that spectrum, Raman bands, may contain the peaks that can best characterize them (Lu et al., 2015). Peaks can be fitted within masked Raman bands to simplify the spectral analysis and is a staple in feature detection engineering. Figure 1 illustrates the main principles of RS.

The primary hurtles for RS microscopy are speed and resolution. Raman signals are inherently weak compared to fluorescent and IR signals, so achieving a large signal-to-noise ratio (SNR) often requires long acquisition times, making it disadvantageous for imaging in living systems, as the biological activity at time scales faster than the acquisition may be missed, and sample movement would interfere with imaging and spatial accuracy of the analyte. Spectral resolution is of paramount interest as well, however, it is difficult for RS to discern the minute differences in chemical structure within macromolecular families and groups thereof. That is, the chemometric methods that separate the label-free Raman spectra of various molecules leaves much to be desired in order to reach a level of sensitivity on par with the likes of fluorescent probes, reporter fusion proteins, immunosorbent assays, and other spectrographic methods. Indeed, RS is just as much about chemometric analysis as it is about spectral acquisition.

Whether the experiment requires high spectral resolution or not, in addition to instrumentation improvement, multivariate analysis is usually used for the differentiation of Raman spectra. In native tissues, for instance, the molecular signature of a metabolite or microstructure may manifest itself in several peaks, while each individual peak may be influenced by the diverse milieu of several molecules. When analyzing a peak, a critical assumption is that any peak may be a linear combination of different peaks (Fereidouni, Bader, & Gerritsen, 2012; Fu & Xie, 2014; Shi et al., 2018). Spectrally unmixing these peaks often requires manual thresholding and identification of Raman bands. The problem is complexed further in the spatial continuum assumption, making these spectra as diverse as snowflakes. There is also the challenge of isoform information hidden in a Raman band. While the primary objective of label-free RS has been the identification of species based on their atomic constituents, minute spectral differences may arise in conformational changes within a bond. For instance, the α-helix isoform of tau protein has a peak at 1654 cm^{-1} while the β-sheet isoform has a peak value of 1,664 cm^{-1} illustrating the significance of torsional bond angle differences alone (Gorantla, Khandelwal, Poddar, & Chinnathambi, 2017). Albeit several peaks of pure substances and even subcellular structures and metabolites are well known, the status quo is far from a unifying theory. Therefore, multivariate analysis methods have been used to decompose spectroscopic profiles into maps of major chemical components. Least squares regression analysis is typically used for mapping samples of known compositions (Fu, Holtom, Freudiger, Zhang, & Xie, 2013; Lee, Moon, Migler, & Cicerone, 2011). For samples with little or no prior knowledge, methods such as principal component analysis (Lin et al., 2011), k-means clustering (Krafft et al., 2009), spectral phasor analysis (Wei et al., 2019), Independent components analysis (Ozeki et al., 2012), multivariate curve resolution analysis (Zhang et al., 2013), as well as in-house-developed algorithm (Masia, Karuna, Borri, & Langbein, 2015; Masia, Pope, Watson, Langbein, & Borri, 2018) have been employed for mapping major components in Raman imaging data. Lately, machine learning (ML) algorithms have been adopted and developed to extract information from Raman spectra (mainly based on pre-known knowledge), such as algorithms developed for assessing expressed human meibum (Alfonso-Garcia et al., 2017), identification of pathogenic bacteria (Ho et al., 2019), and detecting prostate cancer (Lee, Lenferink, Otto, & Offerhaus, 2020). The common techniques used in ML for RS have been timely reviewed by (Lussier, Thibault, Charron, Wallace, & Masson, 2020).

In terms of mammalian cell biology, RS microscopy has its hand in many hats. What has been observed in the recent literature is a gradual transition in application from larger volumes of pure or simple mixtures of materials to smaller volumes of highly complex structures such as cells, organelles, transcriptomes, and metabolomes. Naturally, the instrumentation and analysis may be tailored to the specific level of scope including the tissue, cell, subcellular, and molecular levels. At each level, novel instrumentations and chemometric tools have been generated to help answer each question.

In this review, we first briefly overview the RS modalities and techniques for mammalian tissue and cell imaging. Next, we focus our discussion on the applications of CARS and SRS microscopy in imaging of biological cells and tissues. The developments and applications of spontaneous Raman have been well and thoroughly reviewed by Kumamoto et al. (2018), Smith, Wright, and Ashton (2016), Schie and Huser (2013), and Krafft, Schie, Meyer, Schmitt, and Popp (2016).

2 | MODALITY OF RAMAN IMAGING ON TISSUES

RS imaging on tissues has mostly settled in a diagnostic space in the recent literature. Raman spectra and Raman images may be acquired for such tasks as cancer detection, disease progression, and cell-type or subtype identification and segmentation. X-ray, computed tomography, positron emission tomography, and magnetic resonance imaging exemplify the revolutionary impact of rapid imaging techniques in medicine. As a robust optical method, RS imaging has the potential to rise to the same stature. However, the paradigm of a large instrumentation and small analytical volume does not translate well to the clinical setting. Hand-held Raman devices exist but their resolution and processing capabilities are reduced along with their footprint. For classification applications, this is of little consequence because the utility of a diagnostic tool is often measured by its speed. Screening kits and procedures for several pathogens, cancers, and diseases can be rapidly administered and deliver same-day results. In cancer, for instance, early detection is key to decreasing mortality rates. However, detection methods are tailored to the cancer type, for example, prostate-specific antigen for prostate cancer, fecal occult blood test for colorectal cancer, tumor-associated antigens for breast cancer etc., and often require highly specialized consultation, immunochemical or genetic processing, and lack direct cell-quantification or visualization schema. Typically, the detail, cost, and speed of a test is a zero-sum game. Optical techniques may be able to circumvent the need for expensive immunologic reagents and processing time by directly mapping the spectra to molecular profiles. In as little as 45 s, researchers were able to acquire and categorize the RS of serum from a patient with or without gastric or colon cancer (Ito, Miyazaki, Uragami, Yokoyama, & Inoue, 2019). Nasopharyngeal carcinoma may also be detected in the blood with SERS. In this manner, accuracy, sensitivity, and specificity were found to be 84.4, 85.7, and 78.6%, respectively (Lin et al., 2019). At present, reliable blood tests for cancer are lacking in availability, accuracy, and breadth of application. RS imaging may answer the call for such a sorely needed screening platform.

Another small Raman system was tested in clinical cases of nasopharyngeal carcinoma tissue by capitalizing on fiber optic cables. Rapid endoscopic identification of cancerous

tissue in humans requires more efficient and highly accurate algorithms to be considered a viable platform. The significance of this study lies in the conjugation of chemometric techniques—dubbed genetic algorithms-partial least squares-linear discriminant analysis (GA-PLS-LDA). The addition of the genetically inspired algorithms detects features for the more common PLS-LDA technique and simplifies the analysis of the spectrum. It also provides valuable insight into the biochemical processes in the cell, which are overlooked in algorithms without feature detection. Analysis of the fingerprint and high-wavenumber regions (FP/HW) in the GA-PLS-LDA algorithm had an accuracy, sensitivity, and specificity of 96.76, 87.78, and 100%, respectively—higher than the analogous blood test which may be attributable to the simultaneous unique advantages of both FP and HW Raman tissue spectra (Žuvela et al., 2019). Recent work successfully used resonance Raman techniques (RRS) for brain tumor biopsies (Zhou et al., 2018, 2019), skin cancer detections (Liu et al., 2019), and breast cancer subtype separation (Bendau et al., 2020). Using spontaneous RS to scan colon cells from patients, a k-means clustered image-trained support vector machine was able to diagnose the samples as having Ulcerative Colitis, Crohn's disease, or no irritable bowel disease (IBD). The accuracy, sensitivity, and specificity were 98.90, 99.07, and 98.81%, respectively (Bielecki et al., 2012).

Since there is no universal instrumentation or standard operating procedure in the clinic, structured training data in which a sample's true class juxtaposes its Raman spectrum cannot be translated from the bench. Deep learning (DL) uses artificial neural networks (ANNs) to circumvent this issue, and several designs such as convolutional neural networks (CNNs) in image analysis and data mining have been successfully applied to other spectroscopic techniques such as fluorescence lifetime imaging microscopy (FLIM), and multiphoton light-sheet microscopy (Hollon et al., 2020; Krauß et al., 2018; Suzuki et al., 2019). Taylor et al. (2019) reported a work on high-resolution Raman microscopic detection of follicular thyroid cancer cells with unsupervised ML obtained a more accurate (89.8%) distinction of FTC-133 and Nthy-ori 3–1, in comparison to single-cell spectra (77.6%). Moawad et al. (2019) combined top- and sub-level classifier identified the mallei-complex with high sensitivities (>95%) for the identification of burkholderia mallei and related species with ML-based Raman spectroscopic assay. Other DL toolboxes for image analysis such as Google's AutoML Vision API are readily available and can be utilized well by physicians unfamiliar with ML or DL (Faes et al., 2019).

Multi-cellular Raman analysis ex vivo or in situ has less time and fewer safety constraints. Smaller focal volumes on the order of nanoliters are possible with stationary analytes, machine-assisted focusing, and higher aperture number (NA) objectives. This is commonly referred to as the tight-focusing regime (Zumbusch, Holtom, & Xie, 1999). Greater resolution is also possible with longer pixel dwell times and higher laser power. The sample itself, as well as the instrumentation and analytical techniques, may be manipulated. Syngeneic tumor models, through-skull brain imaging, retinal imaging, and tissue sections of various organs, are recent examples of Raman analytes.

To analyze cell–cell interactions and cell type distributions for contextual biology, one may opt for taking a hyperspectral Raman image using hyperspectral SRS (hsSRS) or hyperspectral CARS (hsCARS) Taking a Raman image with a traditional spontaneous

Raman microscope could require several hours, even days, depending on the pixel density, size of the image, and acquisition settings. Taking a hyperspectral image, in which several Raman images acquired at different shifts are overlaid to create a 3D dataset with a spectrum of intensity at each pixel, would take that even longer. In clinical cases where fast and accurate diagnoses are critical to prognoses, an esoteric and sluggish acquisition is out of the question. In general, coherent scattering approaches such as hsSRS and hsCARS are often employed because they not only have a better SNR, they can capture time-resolve spectral changes to reflect dynamic biological environments, as well as have increased scanning speed for larger samples (Bocklitz et al., 2018; Prince et al., 2017). Video-rate quality of 30 fps or greater, corresponding to pixel dwell times of 100 ns or less, can be achieved while maintaining subcellular resolution, making SRS and CARS attractive to measuring biological cells and dynamics as well (Bocklitz et al., 2018). To reduce noises, spectral filters in CARS systems, or modulating signals for detection >1 MHz in SRS systems can be applied (Prince et al., 2017).

Below are several examples of Raman images of the brain. Morphology, metabolism, and neurodegeneration can be monitored by tuning the SRS microscope's laser to a specific vibrational mode to visualize signals of specific metabolites such as lipids, proteins, and others (Figure 2). Brains may be fixed with 4% paraformaldehyde and physical sectioned, or they may even be visualized in vivo (Saar et al., 2010). RS has already enabled researchers with critical information to optimize clearing methods for the deep imaging of tissue (Chen et al., 2019; Wei et al., 2019). The primary criteria for optimized clearing recipes are preservation of the C-H stretching region. That is, no introduction of peaks by the clearing reagents, and the preservation of protein and lipid signals; 8M urea, followed by 0.2% Triton X-100, increased imaging depth of various brain regions by over 10 times (Wei et al., 2019). This effect is partly due to the small size of urea that allows it to penetrate, partially denature, and hydrate the hydrophobic core of high-refractive index proteins (Hama et al., 2015; Tainaka, Kuno, Kubota, Murakami, & Ueda, 2016; Wei et al., 2019), though in vivo skull clearing recipes exist (Chen et al., 2019). The semantic boundaries can be digitally stained and clearly separated. These may refer to tumors, traumatic brain injury (TBI), or any morphological and metabolic difference that can result in spectral differences (Hollon et al., 2020).

A decisive advantage of RS imaging can be found in the cell-silent region (at wavenumbers 1800–2,800 cm^{-1}) in which few to no molecular species show Raman peaks. Stable isotopes such as ^{2}H and ^{13}C, as well as other compounds, have sharp peaks in this region. However, deuterium labels, for instance, are small, low cost, have a high-incorporation efficiency with little sample preparation, and do not prohibitively disrupt cellular metabolism. Incorporating deuterium into common metabolites such as DNA, lipids, and proteins through fed deuterated water (D_2O) will illuminate the cell silent region at distinct linearly separable peaks. These signals are conveniently distinguished by C-D labeled protein, lipid, DNA/RNA, carbohydrates respectively, which are characteristic of their molecular archetype. After pulse-chasing deuterium, spectral unmixing of these protein, DNA, and lipid signals—both deuterated and hydrogen stretching—can provide clear spatial–temporal metabolic insight in situ (Figure 3a,b) (Shi, Zheng, et al., 2018; Zhang et al., 2019). It should be noted that even with an unchanged molecular structure, deuterated compounds are not wholly

biorthogonal. Toxicity is exhibited when mice achieve a saturation of greater than 20% of body water and the biomechanistic effects are not fully understood (Shi, Zheng, et al., 2018). Incorporation of these labels requires little manual sample preparation and makes RS an excellent metabolic tool. Examples of how these stable isotope labels aid in the Raman imaging of several tissues, namely the adipose, brain, skin, muscle, liver, and pancreas, are illustrated in Figure 3c.

Identification and classification of cells in native environments is another primary front in optical imaging in tissues. Computational histology is a field in its infancy but the ability to digitally stain cells and subcellular components in complex native environments warrants rapid development. The limiting step is the mode of separation. With Raman imaging, it is possible to identify cell types, subtypes, and phenotypes in a label-free manner (Eichberg et al., 2019; Hollon et al., 2020; Lu et al., 2015; Schapiro et al., 2017). DNA, proteins, and lipids have distinct Raman signals in both FP and HW, or C-H stretching, regions such that they can be globally separated.

With improved segmentation potential, hyperspectral Raman images may then be analyzed with further development of novel software tools that were originally developed for other imaging techniques (Pan et al., 2019; Schapiro et al., 2017; Smith et al., 2019). Phasor analysis, for instance, was first applied to FLIM and Förster resonance energy transfer (FRET) data (Clayton, Hanley, & Verveer, 2004; Digman, Caiolfa, Zamai, & Gratton, 2008). It has proven instrumental in multi-color spectrally resolved fluorescent techniques because the width of fluorescence excitation and emission is so wide that spectral overlap limits the number of fluorophores that can be visualized simultaneously (Niehörster et al., 2016; Shen et al., 2020). Today, it can be modified for spectral data and used for fast fit-free single cell segmentation in hyperspectral Raman images as well (Fereidouni et al., 2012; Fu & Xie, 2014). In multi-cellular and tissue analysis, RS microscopy may be supplemented by the conjugation of other optical modalities in an intraoperative approach. It is not uncommon to find optical coherence tomography (OCT), FLIM, and CARS images in the same study (Andreana, Sentosa, Erkkilä, Drexler, & Unterhuber, 2019; Shen et al., 2020).

3 | MODALITY OF RAMAN IMAGING ON CELLS

The homogeneity of a subcellular milieu is no less complex than in tissues. At this level, many research topics require the beam path to be finer, and the spectral analysis to be more sensitive. Fortunately, there are several clever ways to do this. One method involves the development of chemometric algorithms to increase classification ability. PC-LDA, otherwise known as discriminant analysis of principal components (DAPC), can be readily applied to identify phenotypic changes, metabolic activity, and subcellular structures (Fisher et al., 2018; Senger & Robertson, 2020). It can map spectral distinctions monotonically to transcriptomic changes as well (Kobayashi-Kirschvink et al., 2018). Multivariate curve resolution (MCR) is a platform similar to PC-LDA, but makes use of k-means and linear regression. MCR has been demonstrated in hyperspectral Raman images using MATLAB (Wang et al., 2014). Hierarchical cluster analysis, like k-means, clusters spectra on (dis)similarity, but has the advantages of a hierarchical representation of cluster relationships without the need to pre-define the number of clusters. In some cases, pre-processing of

Raman spectra may be prudent. There has been success in the field of feature engineering, where regions of interest are selected for peak-fitting. With simpler spectra and fewer parameters, greater multiplexing of data is possible. In this manner, inter-peak relationships, and even relationships with external parameters, can better classify a spectral profile.

Other methods include manipulation of the hardware to increase SNR, and manipulation of the analyte using labels.

3.1 | Improving label-free resolution

Single cell analysis is especially interested in the spatial and temporal distribution of metabolites and proteins, among others. Researchers have previously turned to fluorophores for this type of study even if a protocol is not already established. Where these fluorescence techniques fall short however is the lack of spatial control of the fluorophore itself in the presence of subcellular compartments that facilitate various niche biochemical reactions. This distribution is at the mercy of natural processes around which the probe must be carefully designed. Whether it is the posttranslational glycosylation of a genetically encoded probe, a localization sequence, or the complexation of a secondary substrate, the biological question at hand may be missed if the fluorophore cannot access the intended region. Occasionally, some questions may be barred from a fluorescent probe. An omnipresent fluorophore may report on its analyte where it is encountered, making the separation of intracellular pools more difficult. As an example, the ratios of labile or “free” heme to total heme has been studied extensively in the context of malaria and metabolic diseases. Genetically encoded fluorescent fusion proteins exhibit FRET quenching in the presence of bound heme in a concentration-dependent manner, but the stability of its expression and the tuning of affinity induce a bit of skepticism in their results (Abshire, Rowlands, Ganesan, So, & Niles, 2017). Subcellular compartments are difficult to assess with these sensors, and conformationally demanding systems such as fusion FRET quenchers require additional binding affinity studies to ensure no non-linear allosteric or non-competitive inhibition. These steps may be avoided by lysing the cell, but live cell studies are preferred in many cases (Atamna, Brahmbhatt, Atamna, Shanower, & Dhahbi, 2015). Intracellular trafficking of heme and other substances such as drugs, may be answered more directly with RS because the spatial control is externally controlled by the stage and/or mirrors. Using the improved sensitivity of hsSRS imaging, researchers can monitor the lysosomatropic sequestration of different types of tyrosine kinase inhibitors (TKIs) quantitatively in live cells (Fu et al., 2014).

Fluorescence microscopy can also be integrated with RS to verify the spatial distribution of the species of interest, and then have the Raman spectra collected. The spanning hypotheses were verified using fluorescent techniques and illustrate the ability of RS imaging to accomplish the same analysis in a label-free manner. These two modalities have been conjugated frequently, but rarely in tandem due to the stark contrast in signal intensity. It is important to measure the fluorescent signal before the Raman signal because the fluorescent signal is sensitive to photobleaching. Recent demonstrations of simultaneous Fourier transformed (FT) two-photon excitation (TPE) and CARS systems have been developed successfully (Lindley et al., 2019). These fluoRaman spectrometers use the same pump,

anti-Stokes, and probe lasers to accomplish complementary single cell metabolic analyses at ultrafast time scales of about 24,000 spectra per second. Combining the fluoRaman principle with flow cytometry, single cell analysis of cells under physical stress was conducted at 10 events per second and revealed that the algae *Haematococcus pluvialis* metabolism of chlorophyll catabolites is augmented under photo-stress during culture. *H. pluvialis* has been studied extensively using FT-TPE for its anti-oxidant, anti-inflammatory, and anti-apoptotic benefits. However, since the autofluorescence of the algae stems from both the fluorescent chlorophyll catabolites (FCC's) and the chlorophyll content, the true fluorescence measurements would not reflect the metabolism of FCC's unless the chlorophyll signals are separated with Raman.

As a standalone platform, however, label-free RS is less capable of imaging at a subcellular level due to a weaker SNR. To visualize small volumes and low concentrations, higher-order RS (HO-CARS) methods have been successfully implemented to achieve greater topographical resolution in tissues (Gong, Zheng, Ma, & Huang, 2019). HO-CARS increases the probability that a photon can report on the vibrational mode of a molecule via harmonic resonance at higher electronic energy levels. In other cases, it makes more sense to increase the amplitude of the driving field using conjugated plasmons. These plasmons which are typically gold or silver nanoparticles (NPs) condense the electric field around them, making it easier for a molecule to respond to the excitation field. This is the principle behind SERS and tip enhanced Raman spectroscopy (TERS). The NPs may either be conjugated physically or chemically to the analyte surface as in the case of SERS, or on the tip of an atomic force microscopy (AFM) probe with which the analyte scanned over as in the case of TERS. In SERS, any chemical bonding of NPs may influence the Raman signal and sometimes lead to a chemical enhancement of signal. This is only possible if the NP plasmons bind to the surface of the analyte and not a substrate with which the analyte interacts. In TERS, single-molecule measurements have come a long way in the past decade, achieving nm resolution. In 2019, a single-stranded DNA can be imaged with single base resolution, establishing a Raman based DNA sequencing method (He et al., 2019). Surface and tip enhanced RS imaging can also be made coherent and achieve the signal enhancement and scanning speed advantages previously described, but moderate photodegradation of conjugated plasmons will occur (Fast & Potma, 2019; Frontiera, Henry, Gruenke, & van Duyne, 2011; Zong et al., 2019). Frontiera commented that this may be well suited to single-cell flow cytometry experiments in which plasmons are continually replenished at each Raman acquisitions.

Advanced modulators can quickly tune a pump and Stokes laser, making it possible to select portions of a Raman spectrum for excitation at highest peak powers. This improves SNR and reduces collection times but requires quick broadband raster scanning and preprocessing to generate masks for the selected spectral regions. This method is called spatial light-modulated SRS (SLM-SRS) (Bae, Zheng, & Huang, 2020) and is similar to adaptive excitation fluorescence microscopy.

3.2 | Improving labeled resolution

Labeled RS methods exist in other forms, in addition to isotopes and dyes, to progress RS microscopy as a standalone platform. While these advancements require more sample preparation, the use of stable isotopes, Raman tags, Raman dyes, and Raman-active NPs is a necessity if the spectral profiles of an analyte have undiscernible features, even for a machine. Compared with deuterium-labeling, alkyne-tags are slightly larger and stronger Raman signals, more powerful for SRS imaging species not abundant in cells with high sensitivity and specificity.

Tags vary in size between less than 1 nm to almost 10 nm. Alkyne and diyne tags are of the smaller variety and are highly Raman-active. Lipid droplets (LDs) and amyloid plaques have been tagged and viewed with alkyne tagged free fatty acids such as 17-octadecynoic acid (17-ODYA) (Wei et al., 2014) though label-free imaging of amyloid plaques has also been demonstrated (Ji et al., 2018). The C–C bond of the alkyne lies sharply in the cell silent region around 2,125 cm^{-1} and can thus be used to visualize lipid synthesis and lipolysis in a similar manner to deuterated samples. A set of 20 Raman-active dyes known collectively as Carbon Rainbow (Carbow) have much sharper signals than fluorescent probes, allowing for more simultaneous imaging. Compared to Manhattan Raman spectroscopy (MARS) dyes, Carbow is engineered to be more evenly distributed along the wavenumber axis (Hu et al., 2018).

Lipid profiles are central to the study of many diseases including Alzheimer', atherosclerosis, diabetes, and cancer (Bukiya, Blank, & Rosenhouse-Dantsker, 2019; Fu et al., 2014; Ji et al., 2018; Kochan et al., 2013; Li et al., 2017; Yi et al., 2018); however, solvent extraction methods and fixation for other imaging modalities can damage the sample, and traditional dyes such as BODIPY and Nile-red can yield non-representative concentration profiles (Greenspan & Fowler, 1985; O'Rourke, Soukas, Carr, & Ruvkun, 2009). Using isotope-labeling coupled SRS imaging, 57 lipid metabolic phenotypes can be separated among deuterated oleic acid fed *Caenorhabditis elegans* (Yu, Mutlu, Liu, & Wang, 2017). CARS and SRS imaging can display variations in lipid droplet size and distribution, and spectroscopy can quantify ratios of saturated, unsaturated, triacylglycerol (TAG), and protein content. Small molecules such as Coenzyme Q (CoQ) can also be synthesized with alkyne tags and pulsed through live cells (Yamakoshi et al., 2012). Most recently, warranted interest in the area of genetically encoded Raman tag development has reached some milestones after a paucity of demonstrable transcriptomic specificity. By encoding a small unnatural amino acid (UAA) analog to pyrrolysine, a phenyl-ring enhanced Raman tag with a strained alkyne functionality, can be incorporated into various proteins and studied in vivo including nuclear histone protein, huntingtin protein, and endoplasmic reticulum membrane protein (Zhang et al., 2018). This reporter is much smaller than the famous green fluorescent protein, yet offers the same level of specificity, albeit a smaller signal intensity.

A Raman probe may refer to a small fiber-optic system ideal for use in endoscopy (Auner et al., 2018) and lower resolution tasks, but herein the term probe will refer to reporter molecules as they are with fluorescent probes and the like. Raman probes also vary greatly in size depending on their intended use. Small molecules such as alkynyl steroids have been referred to as probes in their application to the study of liposomal membrane microdomains

(Yamaguchi et al., 2017) despite their similar size as compared to Raman tags. Large NPs, Raman-active themselves or complexed with compounds on their surface, are also considered probes. When endocytosed, they can be used to separate cells in Raman optofluidic sorters based on their functional properties (Lee et al., 2019). This approach can sort cells with an accuracy of 98.3 ± 1.7% and throughput of 200–500 cells/hr. Label-free optofluidic cell imagers have also been developed using RS and have unprecedented throughput speeds of 140 cells/s and accuracy of 99.5% in pulsed four color signal acquisition (Suzuki et al., 2019). Conjugating the two experiments may pave the way for more detailed supermultiplexed cell sorting capabilities. Several considerations limiting the practical sort speed include viability, flocculation, photo-damage, and analysis speed. Different cells require different orifice sizes, sheath pressures, and laser residence times. Adherent cells grown on culture flasks are especially prone to flocculation and thus careful preparation also plays a role in sorter efficiency. Commercially available electrostatic droplet-based cell sorters often use fluorescence and/or electric current to sort cells based on type, viability, or functionality at rates on the order of 10,000 cells/s. Higher sort accuracies occur at slower sort rates of ~5,000 cells/s, and far exceed the proof of concept speeds for Raman sorters, therefore sheath pressure, cell compartment concentration, and photodamage are lesser concerns (Arnold & Lannigan, 2010).

4 | TYPICAL APPLICATIONS OF COHERENT RAMAN SCATTERING IMAGING ON MAMMALIAN CELLS

Apart from the introduction of Raman-active labeling and clever chemometric algorithms, there is little that can be done to improve the RS platform beyond technological advancements in instrumentation. Several have already been mentioned, however the most popular varieties that offer the largest SNR improvement are the coherent techniques such as CARS and SRS. In the past decades, extensive applications of CARS and SRS imaging techniques have been developed rapidly in cell biology, systems biology, neurology, cancer research, and other fields. We review the typical applications of CARS and SRS in cell imaging, specifically, imaging of lipids, proteins, glucose, and nucleic acids in mammalian cells.

4.1 | CARS imaging in mammalian cell metabolic activities

To enhance Raman signals, CARS microscopy has been developed. CARS uses two synchronized laser beams, the pump beam (ω_p), and the Stokes beam (ω_s). When the frequency difference is resonant to the vibration frequency of a molecule in the cell, four processes occur: coherent Stokes RS, CARS, stimulated Raman gain (SRG) and stimulated Raman loss (SRL). The CARS is generated at the frequency of $2\omega_p-\omega_s$, and has been originally used for label-free imaging of lipids in cells by targeting the strong vibrational of C H bond at ~2,850 cm^{-1} (Nan, Cheng, & Xie, 2003). Studies have also demonstrated quantitative chemical specificity and sensitivity in the detection of proteins and nuclear components in cells. The technical development and advances of CARS have been reviewed in other studies (Camp Jr. & Cicerone, 2015; Cicerone & Camp, 2017; Le, Yue, & Cheng, 2010; Schie, Krafft, & Popp, 2015; Yue & Cheng, 2016), here we review the applications of CARS in imaging lipids, nucleic acids, protein, and glucose in mammalian cells.

4.1.1 | Lipids imaging—Xie's group published the first study of using label-free CARS imaging of LDs in live fibroblast cells (Nan et al., 2003). Their study showed LDs have a high density of C H bonds with high contrast in CARS images at 2,845 cm^{-1}. This study opened a new avenue of employing CARS imaging on lipids metabolism in cells.

Yamaguchi et al. (2007) employed CARS imaging to study the function of comparative gene identification-58 (CGI-58), interacting with perilipin, on lipolysis of LDs in 3T3-L1 cells and mouse hepatoma Hepa1 cells. They observed CGI-58 knockdown did not influence the differentiation of 3T3-L1 adipocytes but led to abnormal accumulation of LDs in 3T3-L1 preadipocytes and Hepa1 cells. Cheng's group has performed a series of studies using CARS on lipids metabolism. They (Le & Cheng, 2009) visualized lipid droplet accumulation, as well as insulin signaling and glucose import simultaneously in single 3T3-L1 cells by using CARS and flow cytometry (Figure 4a). They applied CARS to study lipid accumulation during cancer metastasis in mouse Madison lung carcinoma M109 cells as well in mice (Le, Huff, & Cheng, 2009), and showed intracellular lipid accumulation was due to excess free fatty acids. Using four dimensional CARS live imaging of 3T3-L1 cell, Paar et al. (2012) investigated the dynamics and morphological changes of LDs during stimulated lipolysis and in metabolically active but not proliferating cells. They revealed that LD degradation led to fatty acids overflow, which initiated formation of new LDs.

CARS has also been employed to determine the compositions of LDs in cells. Heinrich et al. (2008) identified saturated and unsaturated fatty acids in 3T3-L1 cells. Rinia et al. (2008) used label-free multiplex CARS microscopy to quantify lipid composition and packing of LDs in 3T3-L1 cells. The distribution of local lipid order and degree of unsaturation in the LDs were revealed (Figure 4b).

4.1.2 | Nucleic acids and protein imaging—CARS has been mainly used for visualizing lipids in cells, organisms, and animals. CARS imaging on protein is usually associated with the studies on nucleic acids. Cheng, Jia, Zheng, and Xie (2002) applied CARS to image mitosis and apoptosis, and map 3D distribution of chromosomes in live mouse NIH 3T3 fibroblast cells. In their first study of CARS imaging on lipid droplets, Nan et al. (2003) also monitored 3T3-L1 cell differentiation process and its relation to lipogenesis. Using multiplex CARS, Kano (2008) visualized filament-like structure in HeLa cells in interphase, Parekh et al. (2010) obtained the first full bandwidth (600–3,200 cm^{-1}) vibrational spectral images from single mouse fibroblasts L929 cells, and identified nuclei with high specificity (Figure 4c). Pliss, Kuzmin, Kachynski, and Prasad (2010) employed CARS for monitoring the apoptosis in HeLa cells. The distributions of DNA and RNA, as well as lipids and proteins, were mapped and a dramatic aggregation of nuclear proteins throughout the cell nucleus during the apoptosis was also observed.

Most recently, using label-free multiplex CARS (MCARS) Guerenne-Del Ben et al. (2019) visualized heterochromatin in human embryonic kidney HEK 293 cells by discerning vibrational signature of condensed proteins, and identified chromosomes and their movement during mitosis, and nuclear structures including nucleoli and nuclear border in interphase of fixed and live HEK 293 cells and live fibroblasts (Figure 4d). Karuna et al. (2019) imaged human osteosarcoma U2OS cell division (prometaphase, anaphase,

telophase) using hyperspectral CARS in the C-H stretching region, and by using a data analysis method they produced 3D images of water, proteins, DNA/proteins mixture, and lipids.

4.2 | SRS imaging in mammalian cell metabolic dynamics

SRS microscopy has emerged as a new imaging technique with fast imaging speed (up to video rate) and high detection sensitivity. It uses two synchronized laser beams, one as the pump beam (ω_p) and the other the Stokes beam (ω_s). When the frequency difference ($\omega_p - \omega_s$) is resonant to the vibration frequency of a molecule in the cell, the Stokes beam intensity increases (stimulated Raman gain, SRG) and the pump beam intensity decreases (stimulated Raman loss, SRL). The SRG or SRL signal undergoes a high-frequency (megahertz) modulation and the modulated SRS signal is extracted by a lock-in amplifier. Compared to spontaneous Raman, SRS imaging offers 1,000 times faster imaging speed (Hu, Wei, Zheng, Shen, & Min, 2014), fine spectral resolution, compatibility with fluorescence, and 3D imaging capability in tissues and animals (Shi, Zheng, et al., 2018). Compared to CARS, SRS is free of non-resonant background, its signal intensity is linearly proportional to molecular concentration, and the spontaneous Raman spectrum is preserved in SRS. These allow for quantitative and straightforward image analysis.

SRS was initially developed as a label free modality for visualizing lipids, protein, nucleic acids, glucose in live cells, tissues, and organisms. Furthermore, a variety of special probes including stable-isotope such as deuterium and ^{13}C, and triple-bond tags such as alkyne and diyne, have been developed and employed to further increase the sensitivity and specificity for SRS imaging in cells that can provide temporal dynamics of chemical bond in addition to spatial distribution. The chemical bonds associated with these tags have sharp Raman peaks in the cell Raman-silent region (1800–2,800 cm^{-1}). Deuterium-labeling and alkyne tags both have been widely adopted for Raman imaging. They can display metabolic activities of labeled species that is not possible using label-free imaging. Deuterium labels are small in size, high incorporation efficient, low cost, and do not perturb metabolism in cells. Compared with deuterium-labeling, alkyne-tags are slightly larger and stronger Raman signals, more powerful for SRS imaging species not abundant in cells with high sensitivity and specificity. The technical development and application of SRS have been reviewed in other studies (Hill & Fu, 2019; Hu, Shi, & Min, 2019; Shen, Hu, & Min, 2019; Yue & Cheng, 2016), here we focus on the applications of SRS in imaging metabolism of protein, lipids, glucose, and DNA in mammalian cells and tissues.

4.2.1 | Lipids imaging—Wang, Min, Freudiger, Ruvkun, and Xie (2011) first applied label-free SRS and successfully detected cellular fat storage in lipid droplets in human embryonic kidney HEK 293 cells. Freudiger et al. (2012) used label free SRS for multicolor imaging of lipids and protein in mouse C_2C_{12} myoblast cell line. Later, Fu, Yu, et al. (2014) employed label-free hyperspectral SRS (hsSRS) for imaging cholesteryl ester (CE) and TAG distributions in mouse macrophage RAW 264.7 cell line and rat hepatic McA-RH7777 cell line. They revealed the predominant storage of CE in macrophage cells and TAG in hepatic cells, respectively.

Using deuterated palmitic acid (d31-PA) with SRS imaging in Chinese hamster ovary (CHO) cells, Zhang, Slipchenko, and Cheng (2011) first observed that oleic acid facilitates the conversion of palmitic acid into lipid droplets. Zhang and Min (2017) also employed d31-PA to directly image fatty acid metabolism in human breast cancer MCF-7 cell line during epithelial–mesenchymal transition (Figure 5a). They found palmitic acid incorporated less into membrane lipids but more into lipid droplets in mesenchymal cells. Combining hsSRS imaging with deuterium-labeling, Fu, Yu, et al. (2014) further observed higher incorporation rate of unsaturated fatty acids than saturated fatty acids in living hepatic McA-RH7777 cells. Using a deuterated cholesterol analog (D38-cholesterol) and hsSRS imaging, Alfonso-García, Pfisterer, Riezman, Ikonen, and Potma (2015) visualized D38-cholesterol esterification and storage in lipid droplets, as well as heterogeneous cholesterol storage, in mouse Y1 adrenal cells. Incorporating SRS imaging with deuterated choline (D_9-choline), Hu et al. (2014) demonstrated live cell imaging of metabolic incorporation of choline-containing metabolites in human cervical cancer HeLa cell line, human bone osteosarcoma U2OS cell line, and HEK 293T cell line (Figure 5c).

Coupling SRS with alkyne-labeled fatty acid, 17-octadecynoic acid (17-ODYA), Wei et al. (2014) observed intracellular formation of lipid droplets, an indication of early atherosclerosis, in human THP-1 macrophages. Chen et al. (2014) developed ^{13}C-edited alkyne tags for three color SRS imaging of DNA, RNA, and fatty acid in live HeLa cells, which facilities multicolor imaging of small biomolecules.

To study cellular activity at a global level, deuterated water (D_2O) was used as a probe and combined together with SRS (DO-SRS) to image de novo lipogenesis in Cos7 and Hela cells (Shi, Zheng, et al., 2018). Unlike probing using deuterium-labeled fatty acids (D-FAs) that would generate more lipid droplets, D_2O does not perturb native metabolism in Cos7 and Hela cells, it can freely diffuse into cells and probe de novo biosynthesis. In addition, they also developed a three-component unmixing algorithm and spectrally decomposed the mixed D-labeled lipids, proteins, and DNA in human fibroblast COS-7 cells (Figure 5b).

4.2.2 | Protein imaging—Label-free SRS was used to visualizing mouse C2C12 myoblast cell line (Freudiger et al., 2012). Coupling SRS with deuterium-labeled amino acids (D-AAs), Wei, Yu, Shen, Wang, and Min (2013) visualized newly synthesized proteins in live HeLa cells, human embryonic kidney HEK 293T cells, and mouse neuroblastoma N2A cells. After optimizing deuterium labeling efficiency, they also imaged de novo protein synthesis and degradation and temporally distinct protein population in live HeLa cells (Wei et al., 2015). Zhang and Min (2017) employed D-AA to image protein synthesis during epithelial–mesenchymal transition in MCF-7 cells. They observed less active anabolism of amino acids after epithelial–mesenchymal transition, indicating slower protein synthesis in mesenchymal cells.

In addition to deuterium labeling, carbon isotope ^{13}C-labeled phenylalanine was coupled with SRS to quantify degradation of overall proteome in HeLa cells (Figure 5d) and HEK 293 T cells (Shen et al., 2014). L-Homopropargylglycine (HPG), an alkyne-tagged analog of methionine, was also used to observe the distribution of newly synthesized proteomes with

spatial enrichment in the nucleoli of HeLa cells under steady state or differentiation condition (Wei et al., 2014).

By in vivo intra-arterial injection of D-AA into mice, Shi, Shen, and Min (2018) imaged the spatial and temporal distributions of newly synthesized proteins in various organs of mouse including brain regions, pancreas, liver, and xeno-grafted tumors. The direct injection into blood stream would distribute D-AA quickly into the organs and increase the labeling process. Applying DO-SRS, Shi, Zheng, et al. (2018) also visualized de novo protein synthesis in a variety of tissues and organs in mice that were administrated with 25% D_2O via drinking water. Compared with deuterium-labeled amino acids (D-AAs), D_2O probing was not tissue biased and generated stronger signal for labeling newly synthesized proteins, it is also cost efficient.

4.2.3 | Glucose imaging—Coupling deuterium-labeled glucose (D7-Glucose) with SRS imaging, Li and Cheng (2015) traced glucose metabolism in living cells including human breast cancer MCF-7, lung cancer A549, prostate cancer PC3 and pancreatic cancer PANC1 cell lines. They observed that D7-Glucose was largely used for lipogenesis in PANC1 cells, in addition, compared to PANC1 cells, PC3 cells showed lower de novo lipogenesis but higher fatty acid uptake. Using D7-Glucose and SRS imaging, Zhang and Min (2017) observed less active anabolism of glucose after epithelial–mesenchymal transition in MCF-7 cells, which indicating slower membrane synthesis, and less glucose incorporation into membrane lipids but more into lipid droplets in mesenchymal cells. Further, Zhang et al. (2019) developed a new imaging platform, spectral tracing of deuterium isotopes (STRIDE), and coupled with D7-Glucose to trace glucose metabolism in HeLa cells (Figure 5e) and mouse tissues. Alkyne-tag was also used in a glucose analog 3-O-propargyl-D-glucose (3-OPG) and coupled with SRS to image glucose uptake activity in HeLa cell line and human glioblastoma U-87 MG cell line (Hu et al., 2015). A much higher alkyne peak was observed in U-87 MG cells than in HeLa cells, indicating an increase glucose uptake activity in U-87 MG cells.

Based on both alkyne and deuterium labeled glucose (^{13}C-labeled 3-OPG and D7-glucose), Long et al. (2018) developed a two-color SRS imaging technique for simultaneously mapping glucose uptake and incorporation activities in multiple cell lines, including U-87 MG cells, PC3 cells, monkey kidney COS-7 cells, MCF-7 cells, and human prostate normal RWPE-1 cells. A higher ratio of glucose incorporation in RWPW-1 cells was observed than in PC-3 cells. Imaging of MCF-7 cells showed that after epithelial-mesenchymal transition, glucose incorporation into cellular lipids dramatically decreased but glucose uptake was not significantly changed.

4.2.4 | Nucleic acids imaging—Zhang et al. (2012) first employed label-free SRS imaging for quantitative mapping nucleic acids distribution in single HEK293 and MCF-7 cells. They showed that cell division can be detected via imaging of DNA condensation. Using label-free SRS imaging, Lu et al. (2015) captured chromosome dynamics during cell division in live HeLa cells. They started from imaging cells in mitotic phase, then imaged interphase cells (Figure 5f). They could visualize chromosomal DNA based on nucleic acids contrast with a high sensitivity.

Coupling 5-ethynyl-2′-deoxyuridine (EdU), an alkyne-tagged thymidine analog, with SRS, Hong et al. (2014) imaged EdU incorporation into HeLa cells during DNA synthesis. Wei et al. (2014) imaged metabolic uptake of EdU for de novo DNA synthesis in HeLa cells during cell cycle. The dividing cells incorporated with EdU could be tracked every 5 min during mitosis. By labeling 5-ethynyl uridine (EU), an alkyne-tagged uridine analog, they visualized RNA transcription and turnover dynamics. The RNA turnover dynamics indicates a short lifetime ~3 h of RNA in live HeLa cells. Using ^{13}C-edited alkyne tags for three color SRS imaging, Chen et al. (2014) visualized DNA, RNA, and fatty acid in live HeLa cells, which provides a new dimension for multicolor imaging of small biomolecules.

5 | OUTLOOK AND CHALLENGES

The evolution of Raman imaging has seen in the last 20 years is astounding. Hardware design and automation, as well as software chemometric analyses have opened many doors in system biological sciences and medicine. Despite its rapid rise in interest, Raman-based optical methods are currently far from standalone. As such, other techniques may pick up where RS (Stiebing et al., 2019) falls short. For example, the massive amount of Raman data needs advanced statistical techniques for dimension reduction clustering and correlation (Hu et al., 2019), the processing and analysis of Raman signals en-masse is better suited to external software equipped with ML and DL capabilities. Several open source and academic licensed packages exist for many needs including single cell segmentation and computational histology.

To study single cells with RS in vivo, microfluidic devices and flow cytometry are often set up in a homebrewed manner. Similarly, optical techniques such as OCT, multiphoton microscopy, and FLIM may be set up for the spatial verification of a species, improved diagnostic performance, or evaluate the effectiveness of a RS experiment. Fluorescence-based techniques are often conjugated due to the higher signal intensities and long-standing use of fluorescent labels. Simultaneous fluoRaman platforms sit on the cutting edge of intraoperative optical techniques.

Development of RS microscopy as a standalone tool progresses in tandem with intraoperative platforms, as new dyes, tags, and NPs offer Raman the improved signal intensity and specificity familiar to fluorescent labeling. Furthermore, sample manipulation such as expansion microscopy and laser modulation such as SLM-SRS are among many other ways to break the diffraction limit and improve spatial resolution. However, this does not rule out the use of complementary techniques. In the pursuit of research, it’s best to get the clearest picture possible. In the practice of medicine, the most pragmatic.

Before RS becomes a clinical tool, pragmatic struggles in the laboratory remain. In practice, the workflow of a taking several Raman spectra or images can be arduous as well. Manual refocusing of the objective, panning of the stage to identify and isolate another subcellular compartment, scanning and stitching large areas, and recalibration of the photodetector can amount to significant human hours. The potential for automation is there, however. Several handheld cameras and smartphones are equipped with real-time level-orienting, perspective-correcting, auto-focusing panoramic and feature detection functionality, and the technology

may be applied to handheld Raman devices in the future (Liao et al., 2018). Indeed, there are several aspects that can be automated in the RS workflow that would improve the user experience. With a more automated workflow, researchers may be more inclined to purchase a Raman system, though even costs of the floated table upon which the RS sits can be prohibitive.

Many labs are eager to disseminate their Raman analytical tools as well, but albeit noble, the arduous task of streamlining and compiling analytical methods is not the primary concern in RS chemometrics. It is the consolidation and dissemination of that knowledge that is so limiting in RS. Establishing a database of RS profiles from various instrumentations and samples will be critical in establishing a library and consensus for more complex identification.

ACKNOWLEDGMENT

L. S. acknowledges support from startup funding from UCSD, NIH U54 pilot CA132378 and 2U54CA132378-11A1.

DISCLOSURE STATEMENT

The authors are not aware of any affiliations, memberships, funding, or financial holdings that might be perceived as affecting the objectivity of this review.

Further Reading

Bendau E, Smith J, Zhang L, Ackerstaff E, Kruchevsky N, Wu B, … Shi L (2020). Distinguishing metastatic triple negative breast cancer from non-metastatic breast cancer using SHG imaging and resonance Raman spectroscopy. Journal of Biophotonics, e202000005 [Epub ahead of print]. [PubMed: 32219996]

REFERENCES

Abshire JR, Rowlands CJ, Ganesan SM, So PTC, & Niles JC (2017). Quantification of labile heme in live malaria parasites using a genetically encoded biosensor. Proceedings of the National Academy of Sciences, 114(11), E2068–E2076.

Alfonso-Garcia A, Paugh J, Farid M, Garg S, Jester JV, & Potma EO (2017). A machine learning framework to analyze hyperspectral stimulated Raman scattering microscopy images of expressed human meibum. Journal of Raman Specroscopy, 48(6), 803–812.

Alfonso-García A, Pfisterer SG, Riezman H, Ikonen E, & Potma EO (2015). D38-cholesterol as a Raman active probe for imaging intracellular cholesterol storage. Journal of Biomedical Optics, 21(6), 061003.

Almehmadi LM, Curley SM, Tokranova NA, Tenenbaum SA, & Lednev IK (2019). Surface enhanced Raman spectroscopy for single molecule protein detection. Scientific Reports, 9(1), 12356. [PubMed: 31451702]

Andreana M, Sentosa R, Erkkilä MT, Drexler W, & Unterhuber A (2019). Depth resolved label-free multimodal optical imaging platform to study morpho-molecular composition of tissue. Photochemical & Photobiological Sciences, 18(5), 997–1008. [PubMed: 30882117]

Arnold LW, & Lannigan J (2010). Practical issues in high-speed cell sorting. Current Protocols in Cytometry, 51(1), 1.24.1–1.24.30.

Atamna H, Brahmbhatt M, Atamna W, Shanower GA, & Dhahbi JM (2015). ApoHRP-based assay to measure intracellular regulatory heme. Metallomics, 7(2), 309–321. [PubMed: 25525887]

Auner GW, Koya SK, Huang C, Broadbent B, Trexler M, Auner Z, … Brusatori MA (2018). Applications of Raman spectroscopy in cancer diagnosis. Cancer and Metastasis Reviews, 37(4), 691–717. [PubMed: 30569241]

Bae K, Zheng W, & Huang Z (2020). Spatial light-modulated stimulated Raman scattering (SLM-SRS) microscopy for rapid multiplexed vibrational imaging. Theranostics, 10(1), 312–322. [PubMed: 31903122]

Bendau E, Smith J, Zhang L, Ackerstaff E, Kruchevsky N, Wu B, … Shi L (2020). Distinguishing metastatic triple-negative breast cancer from nonmetastatic breast cancer using second harmonic generation imaging and resonance Raman spectroscopy. Journal of Biophotonics, e202000005 [Epub ahead of print]. [PubMed: 32219996]

Bernath PF (2005). Spectra of atoms and molecules, 2nd ed. New York, NY: Oxford University Press.

Bielecki C, Bocklitz TW, Schmitt M, Krafft C, Marquardt C, Gharbi A, … Popp J (2012). Classification of inflammatory bowel diseases by means of Raman spectroscopic imaging of epithelium cells. Journal of Biomedical Optics, 17(7), 0760301.

Blackie EJ, Le Ru EC, & Etchegoin PG (2009). Single-molecule surface-enhanced Raman spectroscopy of nonresonant molecules. Journal of the American Chemical Society, 131(40), 14466–14472. [PubMed: 19807188]

Bocklitz T, Meyer T, Schmitt M, Rimke I, Hoffmann F, von Eggeling F, … Popp J (2018). Invited article: Comparison of hyperspectral coherent Raman scattering microscopies for biomedical applications. APL Photonics, 3(9), 092404.

Bukiya AN, Blank PS, & Rosenhouse-Dantsker A (2019). Cholesterol intake and statin use regulate neuronal G protein-gated inwardly rectifying potassium channels. Journal of Lipid Research, 60(1), 19–29. [PubMed: 30420402]

Camp CH Jr., & Cicerone MT (2015). Chemically sensitive bioimaging with coherent Raman scattering. Nature Photonics, 9(5), 295–305.

Chen Y, Liu S, Liu H, Tong S, Tang H, Zhang C, … Wang P (2019). Coherent Raman scattering unravelling mechanisms underlying skull optical clearing for through-skull brain imaging. Analytical Chemistry, 91(15), 9371–9375. [PubMed: 31339298]

Chen Z, Paley DW, Wei L, Weisman AL, Friesner RA, Nuckolls C, & Min W (2014). Multicolor live-cell chemical imaging by isotopically edited alkyne vibrational palette. Journal of the American Chemical Society, 136(22), 8027–8033. [PubMed: 24849912]

Cheng JX, Jia YK, Zheng G, & Xie XS (2002). Laser-scanning coherent anti-stokes Raman scattering microscopy and applications to cell biology. Biophysical Journal, 83(1), 502–509. [PubMed: 12080137]

Cicerone MT, & Camp CH (2017). Histological coherent Raman imaging: A prognostic review. Analyst, 143(1), 33–59. [PubMed: 29098226]

Clayton AHA, Hanley QS, & Verveer PJ (2004). Graphical representation and multicomponent analysis of single-frequency fluorescence lifetime imaging microscopy data. Journal of Microscopy, 213(1), 1–5. [PubMed: 14678506]

Digman MA, Caiolfa VR, Zamai M, & Gratton E (2008). The phasor approach to fluorescence lifetime imaging analysis. Biophysical Journal, 94(2), L14–L16. [PubMed: 17981902]

Eichberg DG, Shah AH, Di L, Semonche AM, Jimsheleishvili G, Luther EM, … Ivan ME (2019). Stimulated Raman histology for rapid and accurate intraoperative diagnosis of CNS tumors: Prospective blinded study. Journal of Neurosurgery, 1–7. [Epub ahead of online].

Faes L, Wagner SK, Fu DJ, Liu X, Korot E, Ledsam JR, … Keane PA (2019). Automated deep learning design for medical image classification by health-care professionals with no coding experience: A feasibility study. The Lancet Digital Health, 1(5), e232–e242.

Fast A, & Potma EO (2019). Coherent Raman scattering with plasmonic antennas. Nano, 8(6), 991–1021.

Fereidouni F, Bader AN, & Gerritsen HC (2012). Spectral phasor analysis allows rapid and reliable unmixing of fluorescence microscopy spectral images. Optics Express, 20(12), 12729–12741. [PubMed: 22714302]

Fisher AK, Carswell WF, Athamneh AIM, Sullivan MC, Robertson JL, Bevan DR, & Senger RS (2018). The Rametrix™ LITE toolbox v1.0 for MATLAB ®. Journal of Raman Spectroscopy, 49(5), 885–896.

Freudiger CW, Pfannl R, Orringer DA, Saar BG, Ji M, Zeng Q, … Young GS (2012). Multicolored stain-free histopathology with coherent Raman imaging. Laboratory Investigation, 92(10), 1492–1502. [PubMed: 22906986]

Frontiera RR, Henry AI, Gruenke NL, & van Duyne RP (2011). Surface-enhanced femtosecond stimulated Raman spectroscopy. The Journal of Physical Chemistry Letters, 2(10), 1199–1203. [PubMed: 26295326]

Fu D, Holtom G, Freudiger C, Zhang X, & Xie XS (2013). Hyperspectral imaging with stimulated Raman scattering by chirped femtosecond lasers. The Journal of Physical Chemistry. *B*, 117(16), 4634–4640. [PubMed: 23256635]

Fu D, & Xie XS (2014). Reliable cell segmentation based on spectral phasor analysis of hyperspectral stimulated Raman scattering imaging data. Analytical Chemistry, 86(9), 4115–4119. [PubMed: 24684208]

Fu D, Yu Y, Folick A, Currie E, Farese RV Jr., Tsai TH, … Wang MC (2014). In vivo metabolic fingerprinting of neutral lipids with hyperspectral stimulated Raman scattering microscopy. Journal of the American Chemical Society, 136(24), 8820–8828. [PubMed: 24869754]

Fu D, Zhou J, Zhu WS, Manley PW, Wang YK, Hood T, … Xie XS (2014). Imaging the intracellular distribution of tyrosine kinase inhibitors in living cells with quantitative hyperspectral stimulated Raman scattering. Nature Chemistry, 6(7), 614–622.

Gong L, Zheng W, Ma Y, & Huang Z (2019). Higher-order coherent anti-stokes Raman scattering microscopy realizes label-free super-resolution vibrational imaging. Nature Photonics, 14, 115–122.

Gorantla NV, Khandelwal P, Poddar P, & Chinnathambi S (2017). Global conformation of Tau protein mapped by Raman spectroscopy. Methods in Molecular Biology, 1523, 21–31. [PubMed: 27975242]

Greenspan P, & Fowler SD (1985). Spectrofluorometric studies of the lipid probe, nile red. Journal of Lipid Research, 26(7), 781–789. [PubMed: 4031658]

Guerenne-Del Ben T, Rajaofara Z, Couderc V, Sol V, Kano H, Leproux P, & Petit J-M (2019). Multiplex coherent anti-stokes Raman scattering s state of chromatin condensation in CH region. Scientific Reports, 9(1), 13862. [PubMed: 31554897]

Hama H, Hioki H, Namiki K, Hoshida T, Kurokawa H, Ishidate F, … Miyawaki A (2015). ScaleS: An optical clearing palette for biological imaging. Nature Neuroscience, 18(10), 1518–1529. [PubMed: 26368944]

He Z, Han Z, Kizer M, Linhardt RJ, Wang X, Sinyukov AM, … Scully MO (2019). Tip-enhanced Raman imaging of single-stranded DNA with single base resolution. Journal of the American Chemical Society, 141(2), 753–757. [PubMed: 30586988]

Heinrich C, Hofer A, Ritsch A, Ciardi C, Bernet S, & Ritsch-Marte M (2008). Selective imaging of saturated and unsaturated lipids by wide-field CARS-microscopy. Optics Express, 16(4), 2699–2708. [PubMed: 18542355]

Hill AH, & Fu D (2019). Cellular imaging using stimulated Raman scattering microscopy. Analytical Chemistry, 91(15), 9333–9342. [PubMed: 31287649]

Ho CS, Jean N, Hogan CA, Blackmon L, Jeffrey SS, Holodniy M, … Dionne J (2019). Rapid identification of pathogenic bacteria using Raman spectroscopy and deep learning. Nature Communications, 10(1), 4927.

Hollon TC, Pandian B, Adapa AR, Urias E, Save AV, Khalsa SSS, … Orringer DA (2020). Near real-time intraoperative brain tumor diagnosis using stimulated Raman histology and deep neural networks. Nature Medicine, 26(1), 52–58.

Hong S, Chen T, Zhu Y, Li A, Huang Y, & Chen X (2014). Live-cell stimulated Raman scattering imaging of alkyne-tagged biomolecules. Angewandte Chemie (International Ed. in English), 53(23), 5827–5831. [PubMed: 24753329]

Hu F, Chen Z, Zhang L, Shen Y, Wei L, & Min W (2015). Vibrational imaging of glucose uptake activity in live cells and tissues by stimulated Raman scattering. Angewandte Chemie (International Ed. in English), 54(34), 9821–9825. [PubMed: 26207979]

Hu F, Shi L, & Min W (2019). Biological imaging of chemical bonds by stimulated Raman scattering microscopy. Nature Methods, 16(9), 830–842. [PubMed: 31471618]

Hu F, Wei L, Zheng C, Shen Y, & Min W (2014). Live-cell vibrational imaging of choline metabolites by stimulated Raman scattering coupled with isotope-based metabolic labeling. Analyst, 139(10), 2312–2317. [PubMed: 24555181]

Hu F, Zeng C, Long R, Miao Y, Wei L, Xu Q, & Min W (2018). Supermultiplexed optical imaging and barcoding with engineered polyynes. Nature Methods, 15(3), 194–200. [PubMed: 29334378]

Ito H, Miyazaki T, Uragami N, Yokoyama N, & Inoue H (2019). Analysis of serum by Raman spectroscopy finds changes in blood metabolites of cancer patients in 45 seconds. Journal of Global Oncology, 5, 57–57.

Ji M, Arbel M, Zhang L, Freudiger CW, Hou SS, Lin D, … Xie XS (2018). Label-free imaging of amyloid plaques in Alzheimer's disease with stimulated Raman scattering microscopy. Science Advances, 4(11), eaat7715. [PubMed: 30456301]

Jones RR, Hooper DC, Zhang L, Wolverson D, & Valev VK (2019). Raman techniques: Fundamentals and Frontiers. Nanoscale Research Letters, 14(1), 231. [PubMed: 31300945]

Kano H (2008). Molecular vibrational imaging of a human cell by multiplex coherent anti-stokes Raman scattering microspectroscopy using a supercontinuum light source. Journal of Raman Spectroscopy, 39(11), 1649–1652.

Karuna A, Masia F, Wiltshire M, Errington R, Borri P, & Langbein W (2019). Label-free volumetric quantitative imaging of the human somatic cell division by hyperspectral coherent anti-stokes Raman scattering. Analytical Chemistry, 91(4), 2813–2821. [PubMed: 30624901]

Kobayashi-Kirschvink KJ, Nakaoka H, Oda A, Kamei K-IF, Nosho K, Fukushima H, … Wakamoto Y (2018). Linear regression links transcriptomic data and cellular Raman spectra. Cell Systems, 7(1), 104–117.e4. [PubMed: 29936183]

Kochan K, Marzec KM, Chruszcz-Lipska K, Jasztal A, Maslak E, Musiolik H, … Baranska M (2013). Pathological changes in the biochemical profile of the liver in atherosclerosis and diabetes assessed by Raman spectroscopy. Analyst, 138(14), 3885–3890. [PubMed: 23515303]

Krafft C, Ramoji AA, Bielecki C, Vogler N, Meyer T, Akimov D, … Popp J (2009). A comparative Raman and CARS imaging study of colon tissue. Journal of Biophotonics, 2(5), 303–312. [PubMed: 19434617]

Krafft C, Schie IW, Meyer T, Schmitt M, & Popp J (2016). Developments in spontaneous and coherent Raman scattering microscopic imaging for biomedical applications. Chemical Society Reviews, 45(7), 1819–1849. [PubMed: 26497570]

Krauß SD, Roy R, Yosef HK, Lechtonen T, El-Mashtoly SF, Gerwert K, & Mosig A (2018). Hierarchical deep convolutional neural networks combine spectral and spatial information for highly accurate Raman-microscopy-based cytopathology. Journal of Biophotonics, 11(10), e201800022. [PubMed: 29781102]

Kumamoto Y, Harada Y, Takamatsu T, & Tanaka H (2018). Label-free molecular imaging and analysis by Raman spectroscopy. Acta Histochemica et Cytochemica, 51(3), 101–110. [PubMed: 30083018]

Le TT, Yue S, & Cheng JX (2010). Shedding new light on lipid biology with coherent anti-stokes Raman scattering microscopy. Journal of Lipid Research, 51(11), 3091–3102. [PubMed: 20713649]

Le TT, & Cheng JX (2009). Single-cell profiling reveals the origin of phenotypic variability in adipogenesis. PLoS One, 4(4), e5189. [PubMed: 19357775]

Le TT, Huff TB, & Cheng JX (2009). Coherent anti-stokes Raman scattering imaging of lipids in cancer metastasis. BMC Cancer, 9, 42. [PubMed: 19183472]

Lee YJ, Moon D, Migler KB, & Cicerone MT (2011). Quantitative image analysis of broadband CARS hyperspectral images of polymer blends. Analytical Chemistry, 83(7), 2733–2739. [PubMed: 21395296]

Li J, & Cheng J-X (2015). Direct visualization of De novo lipogenesis in single living cells. Scientific Reports, 4(1), 6807.

Li J, Condello S, Thomes-Pepin J, Ma X, Xia Y, Hurley TD, … Cheng J-X (2017). Lipid desaturation is a metabolic marker and therapeutic target of ovarian cancer stem cells. Cell Stem Cell, 20(3), 303–314.e5. [PubMed: 28041894]

Liao C-S, Wang P, Huang CY, Lin P, Eakins G, Bentley RT, … Cheng JX (2018). In vivo and in situ spectroscopic imaging by a handheld stimulated Raman scattering microscope. ACS Photonics, 5(3), 947–954.

Lee KS, Palatinszky M, Pereira FC, Nguyen J, Fernandez VI, Mueller AJ, … Stocker R (2019). An automated Raman-based platform for the sorting of live cells by functional properties. Nature Microbiology, 4(6), 1035–1048.

Lee W, Lenferink ATM, Otto C, & Offerhaus HL (2020). Classifying Raman spectra of extracellular vesicles based on convolutional neural networks for prostate cancer detection. Journal of Raman Spectroscopy, 51(2), 293–300.

Lin CY, Suhalim JL, Nien CL, Miljković M.č. D., Diem M, Jester JV, & Potma EO (2011). Picosecond spectral coherent anti-stokes Raman scattering imaging with principal component analysis of meibomian glands. Journal of Biomedical Optics, 16(2), 021104. [PubMed: 21361667]

Lin H, Zhou J, Wu Q, Hung TM, Chen W, Yu Y, … Chen R (2019). Human blood test based on surface-enhanced Raman spectroscopy technology using different excitation light for nasopharyngeal cancer detection. IET Nanobiotechnology, 13(9), 942–945. [PubMed: 31811763]

Lindley M, Hiramatsu K, Nomoto H, Shibata F, Takeshita T, Kawano S, & Goda K (2019). Ultrafast simultaneous Raman-fluorescence spectroscopy. Analytical Chemistry, 91(24), 15563–15569. [PubMed: 31774654]

Liu C, Wu B, Sordillo LA, Boydston-White S, Sriramoju V, Zhang C, … Alfano RR (2019). A pilot study for distinguishing basal cell carcinoma from normal human skin tissues using visible resonance Raman spectroscopy. Journal of Cancer Metastasis and Treatment, 5, 4.

Long R, Zhang L, Shi L, Shen Y, Hu F, Zeng C, & Min W (2018). Two-color vibrational imaging of glucose metabolism using stimulated Raman scattering. Chemical Communications, 54(2), 152–155. [PubMed: 29218356]

Lu F-K, Basu S, Igras V, Hoang MP, Ji M, Fu D, … Xie XS (2015). Label-free DNA imaging in vivo with stimulated Raman scattering microscopy. Proceedings of the National Academy of Sciences, 112(37), 11624–11629.

Lussier F, Thibault V, Charron B, Wallace GQ, & Masson JF (2020). Deep learning and artificial intelligence methods for Raman and surface-enhanced Raman scattering. TrAC Trends in Analytical Chemistry, 124, 115796.

Masia F, Pope I, Watson P, Langbein W, & Borri P (2018). Bessel-beam hyperspectral CARS microscopy with sparse sampling: Enabling high-content high-throughput label-free quantitative chemical imaging. Analytical Chemistry, 90(6), 3775–3785. [PubMed: 29505230]

Masia F, Karuna A, Borri P, & Langbein W (2015). Hyperspectral image analysis for CARS, SRS, and Raman data. Journal of Raman Specroscopy, 46(8), 727–734.

Moawad AA, Silge A, Bocklitz T, Fischer K, Rösch P, Roesler U, … Neubauer H (2019). A machine learning-based Raman spectroscopic assay for the identification of *Burkholderia mallei* and related species. Molecules, 24(24), 4516.

Nan X, Cheng JX, & Xie XS (2003). Vibrational imaging of lipid droplets in live fibroblast cells with coherent anti-stokes Raman scattering microscopy. Journal of Lipid Research, 44(11), 2202–2208. [PubMed: 12923234]

Niehörster T, Löschberger A, Gregor I, Krämer B, Rahn HJ, Patting M, … Sauer M (2016). Multi-target spectrally resolved fluorescence lifetime imaging microscopy. Nature Methods, 13(3), 257–262. [PubMed: 26808668]

O'Rourke EJ, Soukas AA, Carr CE, & Ruvkun G (2009). *C. elegans* major fats are stored in vesicles distinct from lysosome-related organelles. Cell Metabolism, 10(5), 430–435. [PubMed: 19883620]

Ozeki Y, Umemura W, Otsuka Y, Satoh S, Hashimoto H, Sumimura K, … Itoh K (2012). High-speed molecular spectral imaging of tissue with stimulated Raman scattering. Nature Photonics, 6(12), 845–851.

Pan C, Schoppe O, Parra-Damas A, Cai R, Todorov MI, Gondi G, … Ertürk A (2019). Deep learning reveals cancer metastasis and therapeutic antibody targeting in the entire body. Cell, 179(7), 1661–1676.e19. [PubMed: 31835038]

Paar M, Jüngst C, Steiner NA, Magnes C, Sinner F, Kolb D, … Wolinski H (2012). Remodeling of lipid droplets during lipolysis and growth in adipocytes. The Journal of Biological Chemistry, 287(14), 11164–11173. [PubMed: 22311986]

Parekh SH, Lee YJ, Aamer KA, & Cicerone MT (2010). Label-free cellular imaging by broadband coherent anti-stokes Raman scattering microscopy. Biophysical Journal, 99(8), 2695–2704. [PubMed: 20959111]

Pliss A, Kuzmin AN, Kachynski AV, & Prasad PN (2010). Biophotonic probing of macromolecular transformations during apoptosis. Proceedings of the National Academy of Sciences of the United States of America, 107(29), 12771–12776. [PubMed: 20615987]

Prince RC, Frontiera RR, & Potma EO (2017). Stimulated Raman scattering: From bulk to nano. Chemical Reviews, 117(7), 5070–5094. [PubMed: 27966347]

Rinia HA, Burger KNJ, Bonn M, & Müller M (2008). Quantitative label-free imaging of lipid composition and packing of individual cellular lipid droplets using multiplex CARS microscopy. Biophysical Journal, 95(10), 4908–4914. [PubMed: 18689461]

Saar BG, Freudiger CW, Reichman J, Stanley CM, Holtom GR, & Xie XS (2010). Video-rate molecular imaging in vivo with stimulated Raman scattering. Science, 330(6009), 1368–1370. [PubMed: 21127249]

Schapiro D, Jackson HW, Raghuraman S, Fischer JR, Zanotelli VRT, Schulz D, … Bodenmiller B (2017). histoCAT: Analysis of cell phenotypes and interactions in multiplex image cytometry data. Nature Methods, 14(9), 873–876. [PubMed: 28783155]

Schie IW, & Huser T (2013). Methods and applications of Raman microspectroscopy to single-cell analysis. Applied Spectroscopy, 67(8), 813–828. [PubMed: 23876720]

Schie IW, Krafft C, & Popp J (2015). Applications of coherent Raman scattering microscopies to clinical and biological studies. Analyst, 140(12), 3897–3909. [PubMed: 25811305]

Senger RS, & Robertson JL (2020). The Rametrix ™ PRO toolbox v1.0 for MATLAB ®. PeerJ, 8, e8179. [PubMed: 31934499]

Shen Y, Xu F, Wei L, Hu F, & Min W (2014). Live-cell quantitative imaging of proteome degradation by stimulated Raman scattering. Angewandte Chemie (International Ed. in English), 53(22), 5596–5599. [PubMed: 24737659]

Shen Y, Hu F, & Min W (2019). Raman imaging of small biomolecules. Annual Review of Biophysics, 48(1), 347–369.

Shen B, Yan J, Wang S, Zhou F, Zhao Y, Hu R, … Liu L (2020). Label-free whole-colony imaging and metabolic analysis of metastatic pancreatic cancer by an autoregulating flexible optical system. Theranostics, 10(4), 1849–1860. [PubMed: 32042340]

Shi L, Shen Y, & Min W (2018). Visualizing protein synthesis in mice with in vivo labeling of deuterated amino acids using vibrational imaging. APL Photonics, 3(9), 092401.

Shi L, Zheng C, Shen Y, Chen Z, Silveira ES, Zhang L, … Min W (2018). Optical imaging of metabolic dynamics in animals. Nature Communications, 9(1), 2995.

Smith R, Wright KL, & Ashton L (2016). Raman spectroscopy: An evolving technique for live cell studies. Analyst, 141(12), 3590–3600. [PubMed: 27072718]

Smith JT, Yao R, Sinsuebphon N, Rudkouskaya A, Un N, Mazurkiewicz J, … Intes X (2019). Fast fit-free analysis of fluorescence lifetime imaging via deep learning. Proceedings of the National Academy of Sciences, 116(48), 24019–24030.

Stiebing C, Schie IW, Knorr F, Schmitt M, Keijzer N, Kleemann R, … Popp J (2019). Nonresonant Raman spectroscopy of isolated human retina samples complying with laser safety regulations for in vivo measurements. Neurophotonics, 6(4), 041106. [PubMed: 31482104]

Suzuki Y, Kobayashi K, Wakisaka Y, Deng D, Tanaka S, Huang C-J, … Ozeki Y (2019). Label-free chemical imaging flow cytometry by high-speed multicolor stimulated Raman scattering. Proceedings of the National Academy of Sciences, 116(32), 15842–15848.

Tainaka K, Kuno A, Kubota SI, Murakami T, & Ueda HR (2016). Chemical principles in tissue clearing and staining protocols for whole-body cell profiling. Annual Review of Cell and Developmental Biology, 32, 713–741.

Taylor JN, Mochizuki K, Hashimoto K, Kumamoto Y, Harada Y, Fujita K, & Komatsuzaki T (2019). High-resolution Raman microscopic detection of follicular thyroid cancer cells with unsupervised machine learning. The Journal of Physical Chemistry. B, 123(20), 4358–4372. [PubMed: 31035762]

Wang MC, Min W, Freudiger CW, Ruvkun G, & Xie XS (2011). RNAi screening for fat regulatory genes with SRS microscopy. Nature Methods, 8(2), 135–138. [PubMed: 21240281]

Wang P, Liu B, Zhang D, Belew MY, Tissenbaum HA, & Cheng JX (2014). Imaging lipid metabolism in live *Caenorhabditis elegans* using fingerprint vibrations. Angewandte Chemie International Edition, 53(44), 11787–11792. [PubMed: 25195517]

Wei L, Yu Y, Shen Y, Wang MC, & Min W (2013). Vibrational imaging of newly synthesized proteins in live cells by stimulated Raman scattering microscopy. Proceedings of the National Academy of Sciences of the United States of America, 110(28), 11226–11231. [PubMed: 23798434]

Wei L, Hu F, Shen Y, Chen Z, Yu Y, Lin CC, … Min W (2014). Live-cell imaging of alkyne-tagged small biomolecules by stimulated Raman scattering. Nature Methods, 11(4), 410–412. [PubMed: 24584195]

Wei L, Shen Y, Xu F, Hu F, Harrington JK, Targoff KL, & Min W (2015). Imaging complex protein metabolism in live organisms by stimulated Raman scattering microscopy with isotope labeling. ACS Chemical Biology, 10(3), 901–908. [PubMed: 25560305]

Wei M, Shi L, Shen Y, Zhao Z, Guzman A, Kaufman LJ, … Min W (2019). Volumetric chemical imaging by clearing-enhanced stimulated Raman scattering microscopy. Proceedings of the National Academy of Sciences, 116(14), 6608–6617.

Yamaguchi T, Omatsu N, Morimoto E, Nakashima H, Ueno K, Tanaka T, … Osumi T (2007). CGI-58 facilitates lipolysis on lipid droplets but is not involved in the vesiculation of lipid droplets caused by hormonal stimulation. Journal of Lipid Research, 48(5), 1078–1089. [PubMed: 17308334]

Yamaguchi S, Matsushita T, Izuta S, Katada S, Ura M, Ikeda T, … Okamoto A (2017). Chemically-activatable alkyne-tagged probe for imaging microdomains in lipid bilayer membranes. Scientific Reports, 7(1), 41007. [PubMed: 28117375]

Yamakoshi H, Dodo K, Palonpon A, Ando J, Fujita K, Kawata S, & Sodeoka M (2012). Alkyne-tag Raman imaging for visualization of mobile small molecules in live cells. Journal of the American Chemical Society, 134(51), 20681–20689. [PubMed: 23198907]

Yi M, Li J, Chen S, Cai J, Ban Y, Peng Q, … Xiang B (2018). Emerging role of lipid metabolism alterations in cancer stem cells. Journal of Experimental & Clinical Cancer Research, 37(1), 118. [PubMed: 29907133]

Yue S, & Cheng JX (2016). Deciphering single cell metabolism by coherent Raman scattering microscopy. Current Opinion in Chemical Biology, 33, 46–57. [PubMed: 27288951]

Yu Y, Mutlu AS, Liu H, & Wang MC (2017). High-throughput screens using photo-highlighting discover BMP signaling in mitochondrial lipid oxidation. Nature Communications, 8(1), 865.

Zhang D, Slipchenko MN, & Cheng JX (2011). Highly sensitive vibrational imaging by femtosecond pulse stimulated Raman loss. Journal of Physical Chemistry Letters, 2(11), 1248–1253. [PubMed: 21731798]

Zhang X, Roeffaers MBJ, Basu S, Daniele JR, Fu D, Freudiger CW, … Xie XS (2012). Label-free live-cell imaging of nucleic acids using stimulated Raman scattering microscopy. ChemPhysChem, 13(4), 1054–1059. [PubMed: 22368112]

Zhang D, Wang P, Slipchenko MN, Ben-Amotz D, Weiner AM, & Cheng JX (2013). Quantitative vibrational imaging by hyperspectral stimulated Raman scattering microscopy and multivariate curve resolution analysis. Analytical Chemistry, 85(1), 98–106. [PubMed: 23198914]

Zhang L, & Min W (2017). Bioorthogonal chemical imaging of metabolic changes during epithelial-mesenchymal transition of cancer cells by stimulated Raman scattering microscopy. Journal of Biomedical Optics, 22(10), 1–7.

Zhang J, Yan S, He Z, Ding C, Zhai T, Chen Y, … Wang P (2018). Small unnatural amino acid carried Raman tag for molecular imaging of genetically targeted proteins. The Journal of Physical Chemistry Letters, 9(16), 4679–4685. [PubMed: 30067370]

Zhang L, Shi L, Shen Y, Miao Y, Wei M, Qian N, … Min W (2019). Spectral tracing of deuterium for imaging glucose metabolism. Nature Biomedical Engineering, 3(5), 402–413.

Zhou Y, Liu CH, Wu B, Zhang C, Yu X, Cheng G, … Alfano RR (2018). Invited article: Molecular biomarkers characterization for human brain glioma grading using visible resonance Raman spectroscopy. APL Photonics, 3(12), 120802.

Zhou Y, Liu C-H, Wu B, Yu X, Cheng G, Zhu K, … Alfano RR (2019). Optical biopsy identification and grading of gliomas using label-free visible resonance Raman spectroscopy. Journal of Biomedical Optics, 24(9), 1–12.

Zumbusch A, Holtom GR, & Xie XS (1999). Three-dimensional vibrational imaging by coherent anti-stokes Raman scattering. Physical Review Letters, 82(20), 4142–4145.

Zong C, Premasiri R, Lin H, Huang Y, Zhang C, Yang C, … Cheng J-X (2019). Plasmon-enhanced stimulated Raman scattering microscopy with single-molecule detection sensitivity. Nature Communications, 10(1), 5318.

Žuvela P, Lin K, Shu C, Zheng W, Lim CM, & Huang Z (2019). Fiber-optic Raman spectroscopy with nature-inspired genetic algorithms enhances real-time in vivo detection and diagnosis of nasopharyngeal carcinoma. Analytical Chemistry, 91(13), 8101–8108. [PubMed: 31135136]

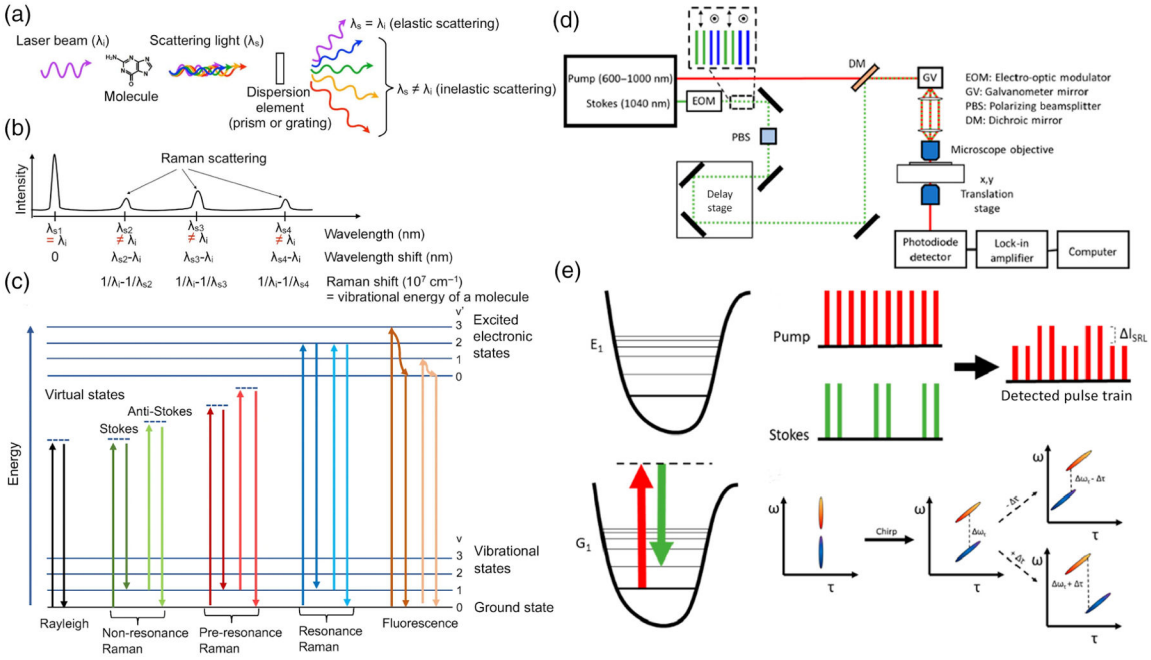

FIGURE 1.

(a) A diagram showing visible monochromatic laser light scattered by a molecule. Inelastic scattering can be recorded and displayed on a spectrum. (b) An example spectrum of observed Raman scattering with arbitrary intensity units on the vertical axis and Raman shifts in wavenumbers or centimeters inversed on the horizontal axis, displaying the relative incidence of scattered light of certain wavelength and therefore bond vibrations in the sample molecule (Kumamoto, Harada, Takamatsu, & Tanaka, 2018). (c) An electronic energy diagram depicting the difference between Rayleigh scattering (filtered out of Raman systems), RS in green, and electronic pre-resonance (EPR) in red, and resonant Raman in blue (Reprinted from (Auner et al., 2018) under the terms of the Creative Commons Attribution 4.0 International License http://creativecommons.org/licenses/by/4.0/). (d) An illustration of a stimulated Raman system including a Stokes beam to make inelastically scattered light coherent to aid detection and boost intensity. (e) Energy diagram and basis of how a stimulated system's laser source is comprised of a Pump and Stokes beam overlaid in space and time to create a stimulated Raman gain/loss and augment the intensity of a Raman signal is shown (Adapted with permission from Hill and Fu (2019). Copyright 2019 American Chemical Society)

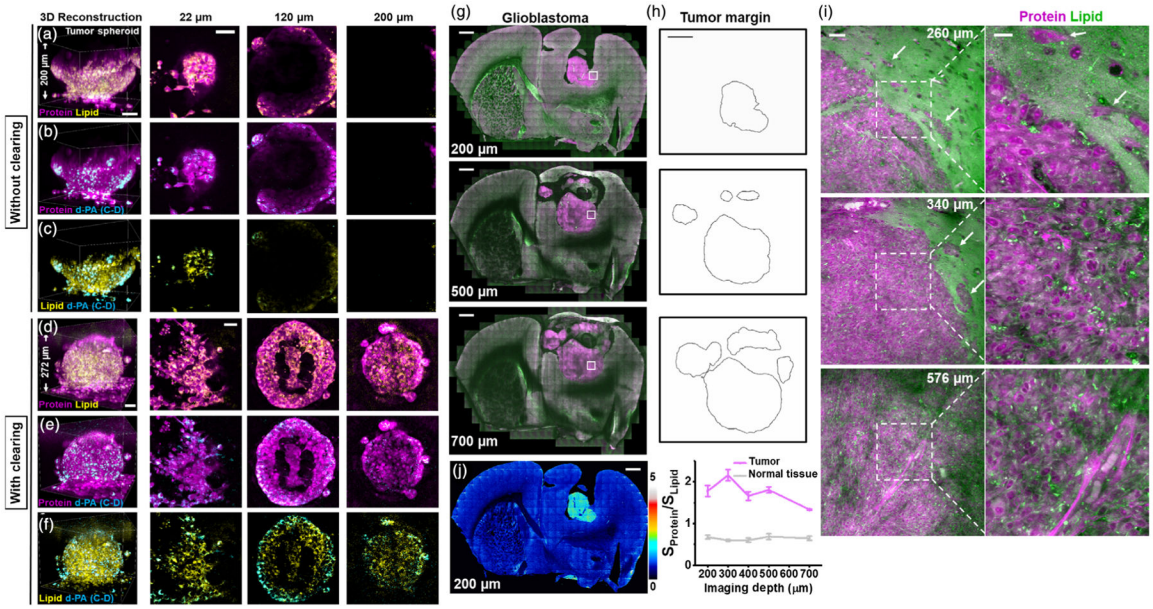

FIGURE 2.

Stimulated Raman imaging of cleared tissue. (a–f) Label-free protein and lipid channels of a 3D MCF-10AHras tumor spheroid overlapped and independently imaged at various depths with and without clearing. (g) Through-skull imaging of a glioblastoma with (h) tumor boundaries clearly shown. (i) Computational histology of the tumor/brain interface using protein and lipid channels of the white boxed regions in (g) at specified imaging depths. (Scale Bars: 1 mm (g,h and j), 50 μm (I-left), 20 μm (I-right)). (j) Protein/lipid ratiometric image at 100 μm imaging depth. (a–j, Adapted with permission from Wei et al. (2019). Copyright 2019 National Academy of Sciences)

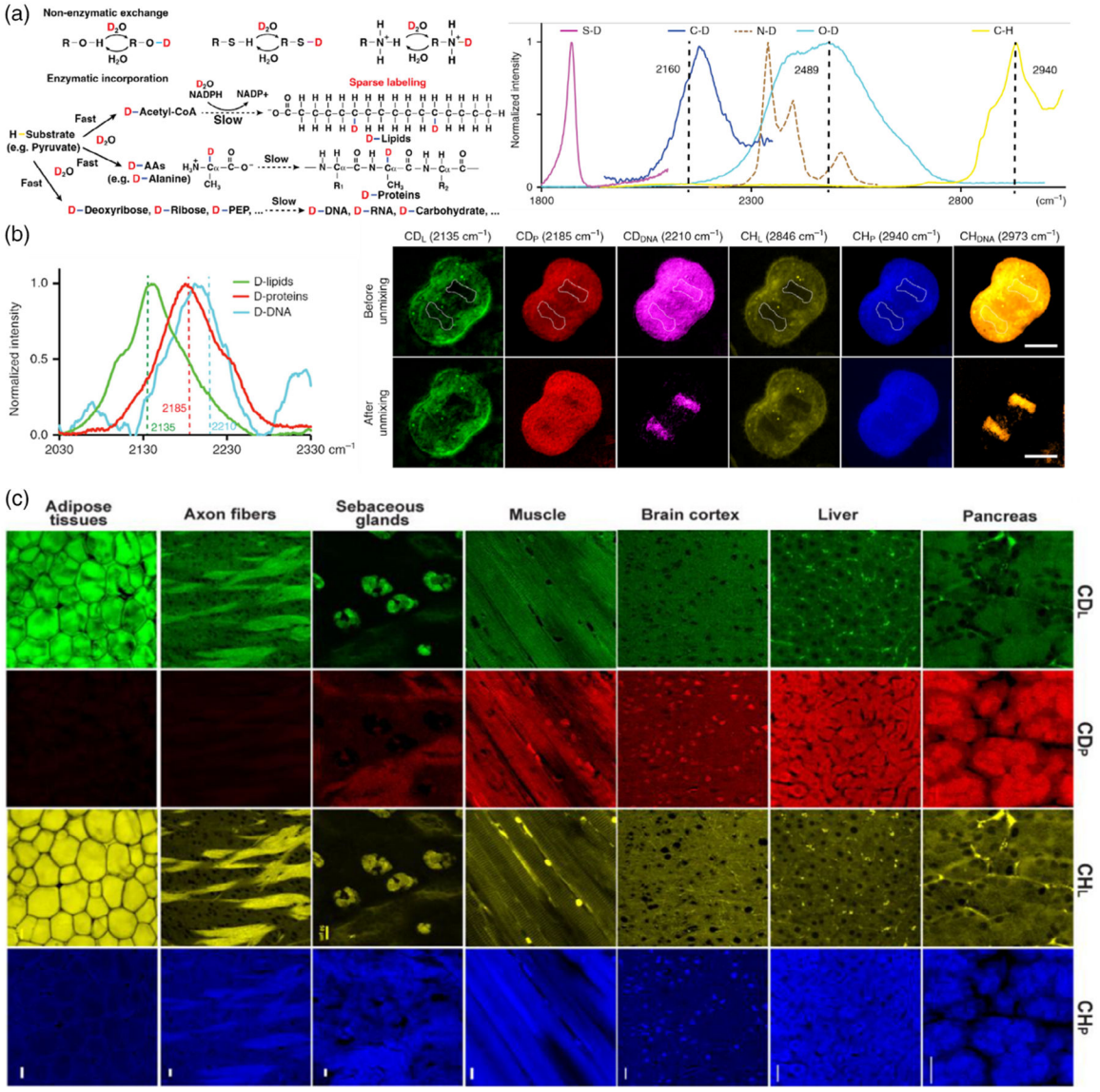

FIGURE 3.

Deuterium as a stable-isotope Raman tag. (a) Proposed mechanisms of incorporation of Deuterium (Left) and how this incorporation manifests in the cell-silent region (Right). (b) Normalized CD_L CD_P and CD_{DNA} signals (Left) used to unmix SRS images (Right). Cell-silent region signals appear as viable as the signals used from the C-H stretching region. (c) SRS images of various tissues after enzymatic incorporation of a deuterium from heavy water in animal feed (Adapted with permission from Shi, Zheng, et al. (2018). Copyright 2018 Springer Nature)

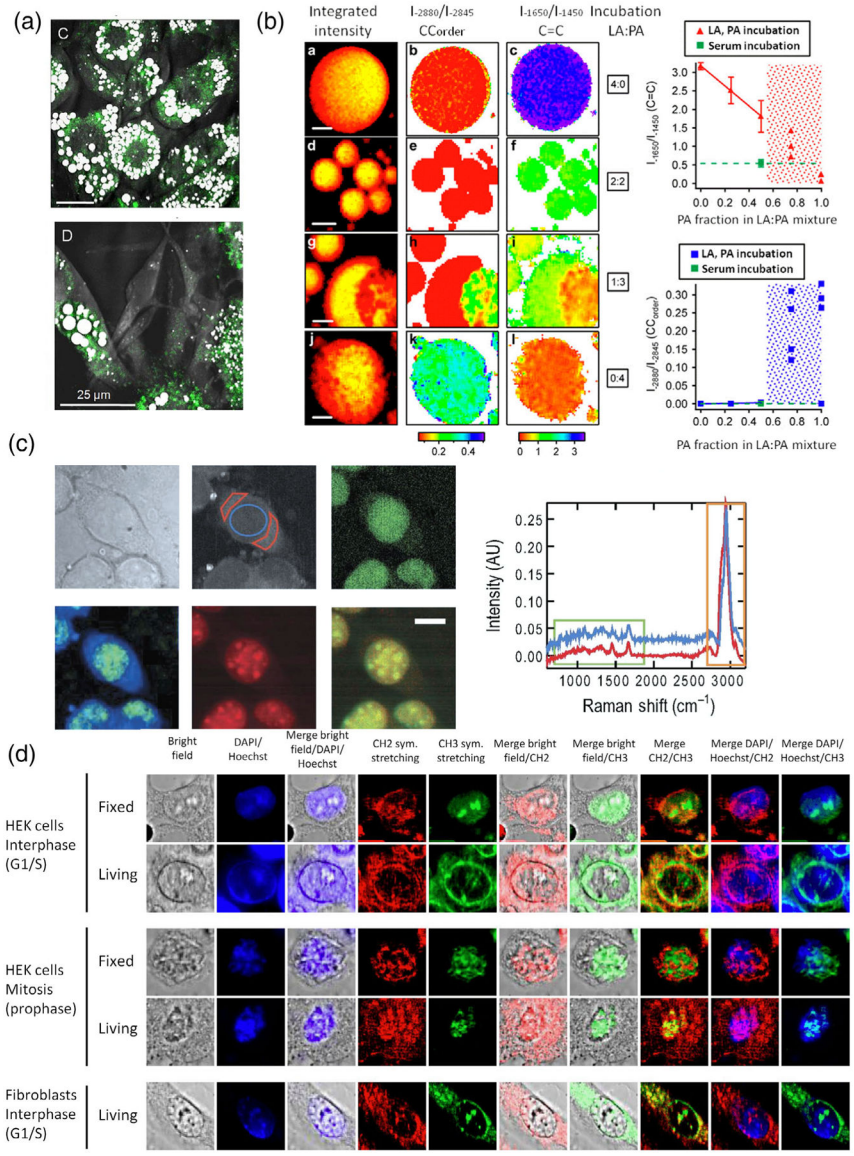

FIGURE 4.

Application of CARS imaging in mammalian cells. (a) Imaging reveals strong glucose import in lipid-rich cells (left) and lipid-poor cells (right) (Adapted with permission from Le and Cheng (2009) under the terms of the Creative Commons Attribution 4.0 International License http://creativecommons.org/licenses/by/4.0/). (b) Lipid-droplet composition and packing dependent on incubation medium (Reprinted with permission from Rinia, Burger, Bonn, and Müller (2008). Copyright 2008 The Biophysical Society. Published by Elsevier Inc. All rights reserved). (c) Imaging of L929 cell nuclei (Adapted with permission from Parekh, Lee, Aamer, and Cicerone (2010). Copyright 2010 Biophysical Society. Published by Elsevier Inc. All rights reserved). (d) Analysis of interphase and mitotic, stained, fixed and living, HEK293 cells and fibroblasts (Adapted with permission from Guerenne-Del Ben et al. (2019) under the terms of the Creative Commons Attribution 4.0 International License http://creativecommons.org/licenses/by/4.0/)

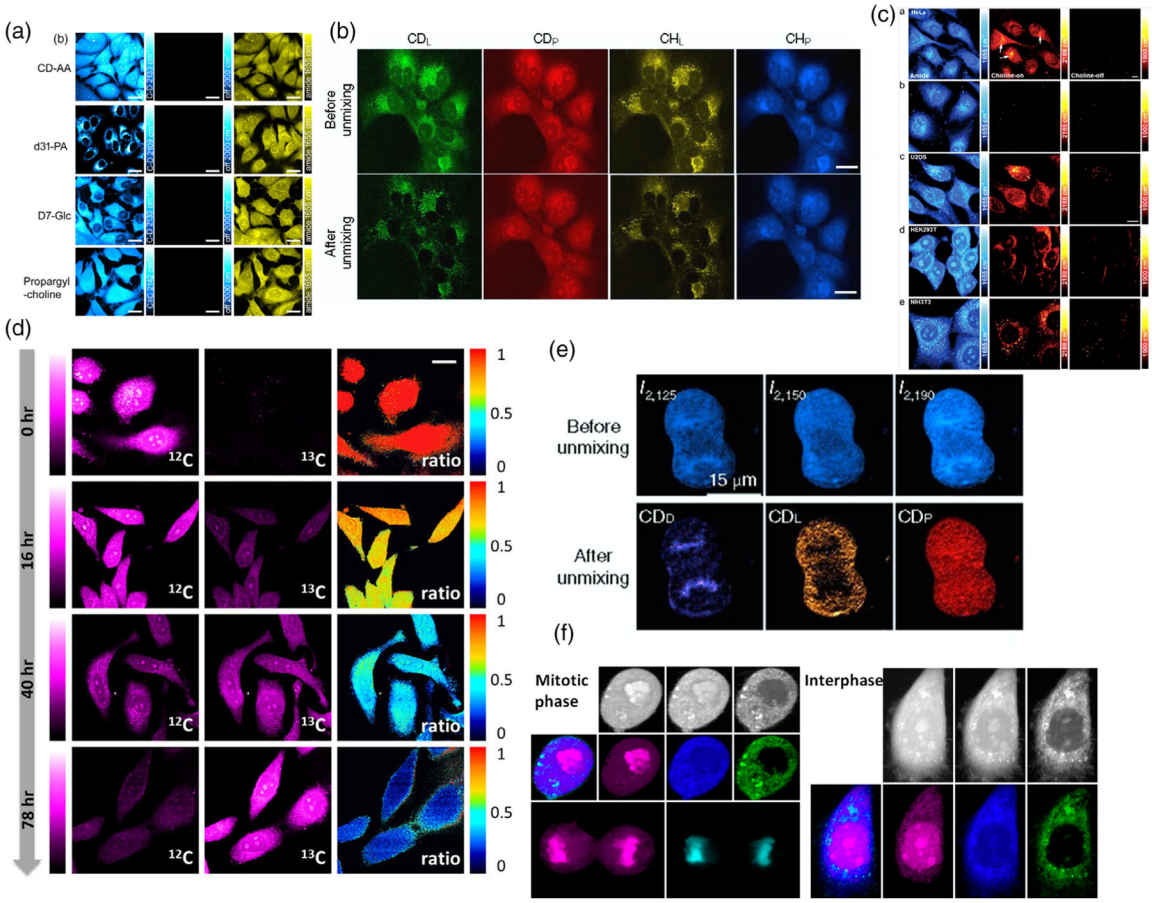

FIGURE 5.

Application of SRS imaging in mammalian cells. (a) MCF-7 cells cultured in mediums with metabolic labels (Zhang & Min, 2017, 2020). (b) Spectral unmixing of D-labeled lipids, proteins, and DNA in Cos7 cells with DO-SRS (Adapted with permission from Shi, Zheng, et al. (2018). Copyright 2018 Springer Nature). (c) D9-choline-containing metabolites in different cancer and embryonic cell lines (Reproduced with permission from Ji et al. (2018). Copyright 2018 The Royal Society of Chemistry). (d) SRS images reveal protein degradation kinetics in HeLa cells (Reproduced with permission from Shen, Xu, Wei, Hu, and Min (2014). Copyright 2014 WILEY-VCH Verlag GmbH & Co. KGaA, Weinheim). (e) Multiplexed imaging of macromolecule biosynthesis activity using STRIDE of [D7]-glucose. Images of a [D7]-glucose-labeled mitotic HeLa cell before and after unmixing (Zhang et al., 2019). (f) Label-free SRS imaging of DNA (magenta), protein (blue), and lipids (green) in live cells in mitotic phase and interphase (Adapted with permission from Lu et al. (2015). Copyright 2015 National Academy of Sciences